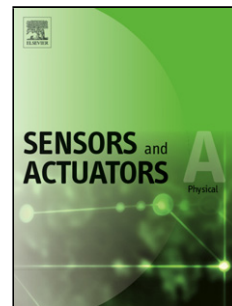


Accepted Manuscript

Title: Modeling the Analog Response of Passive Infrared Sensor

Author: Bodhibrata Mukhopadhyay Seshan Srirangarajan
Subrat Kar



PII: S0924-4247(17)32152-0
DOI: <https://doi.org/doi:10.1016/j.sna.2018.05.002>
Reference: SNA 10763

To appear in: *Sensors and Actuators A*

Received date: 30-11-2017
Revised date: 3-4-2018
Accepted date: 3-5-2018

Please cite this article as: Bodhibrata Mukhopadhyay, Seshan Srirangarajan, Subrat Kar, Modeling the Analog Response of Passive Infrared Sensor, <![CDATA[Sensors & Actuators: A. Physical]]> (2018), <https://doi.org/10.1016/j.sna.2018.05.002>

This is a PDF file of an unedited manuscript that has been accepted for publication. As a service to our customers we are providing this early version of the manuscript. The manuscript will undergo copyediting, typesetting, and review of the resulting proof before it is published in its final form. Please note that during the production process errors may be discovered which could affect the content, and all legal disclaimers that apply to the journal pertain.

Modeling the Analog Response of Passive Infrared Sensor

Bodhibrata Mukhopadhyay^a, Seshan Srirangarajan^{a,b}, Subrat Kar^{a,b}

^a*Department of Electrical Engineering, Indian Institute of Technology Delhi, New Delhi, India*

^b*Bharti School of Telecommunication Technology and Management, Indian Institute of Technology Delhi, New Delhi, India*

Abstract

Passive infrared (PIR) sensors are sensitive to infrared (IR) rays and are mostly used for motion detection. In this paper we propose a mathematical model that enables better understanding of the analog response of the PIR sensor, the Fresnel lens, and the associated electronic circuitry. The proposed model relates the sensor's analog output waveform to the width of sensing element, and speed of movement and distance of the subject from the PIR sensor. Experiments were performed to capture the sensor's analog output waveform corresponding to the subject's movement through the sensor's field of view (FoV) at different distances, and the relationship of the sensor's peak-to-peak output voltage with distance and speed of the subject. The simulation results are shown to match reasonably well with the experimental results.

Keywords: Passive infrared sensor, sensor modeling, Fresnel lens

1. Introduction

Passive infrared sensors have gained in popularity due to the massive development of embedded systems and the Internet of Things (IoT). They are used as a low cost motion sensor that responds when an infrared (IR) emitting subject (humans or animals) passes through its field of view (FoV). Applications of PIR sensor range from monitoring wild life activity [1] to human identification [2], and are used in both indoor and outdoor environments. Most often the digital output of the PIR sensor is used, however there have also been some attempts at exploring the raw or analog output [3, 4, 5, 6, 7].

Zappi et al. [3] extracted features from the analog output of PIR sensors to predict the direction of movement of a subject and count the number of subjects in its FoV. They placed three PIR sensors in a row with different orientations. Two scenarios were considered: (i) three people walking in a line, and (ii) three people walking side by side. Using features, such as the number of peak pairs, direction of the first peak, duration of the second peak, from the analog output of the PIR sensors the authors achieved an accuracy of 100% in predicting direction of movement and an accuracy of 89% in predicting the number of people. In a follow-up paper [8], they used two PIR sensors to estimate the direction of movement and the zone through which the subject had moved along a hallway. Machine learning techniques were applied on features extracted

Email addresses: bodhibrata@gmail.com (Bodhibrata Mukhopadhyay), seshan@ee.iitd.ac.in (Seshan Srirangarajan), subrat@ee.iitd.ac.in (Subrat Kar)

from the analog output of PIR sensors. The sensors were placed facing each other on opposite walls of the hallway. The authors evaluated their system using two types of feature vectors: (i) raw features (analog output and duration from the sensors), and (ii) relative features (ratio of features from the two sensors). They achieved higher accuracy using raw features, however using raw features requires higher computational resources and memory.

PIR sensors have been used in biomedical applications such as gait velocity estimation [4], human identification [2], and activity monitoring [9]. There have been attempts at using PIR sensors in outdoor applications as well despite their inability to work in the presence of direct sunlight. Xin et al. [5] classified vehicles, humans, and animals with PIR and seismic sensors. PIR sensors have also been employed for localization and tracking of humans. Authors in [6] modulated the sensing area of PIR sensors for the tracking of humans. Their technique can track up to two people at a time by using a PIR tower with an array of four PIR sensors placed vertically. The FoV of the sensors is divided into sectors, and by modulating the sensing area they were successful in determining the sector in which the subject was present. Using this information they were able to localize the subject. For refining the position of the subject further they used grid approximation and Kalman filtering. They extended their work for the identification of individuals on the basis of the radiated body heat using PIR sensors [10].

Narayana et al. [7] used the analog output of PIR sensors to classify subjects on the basis of their height and width. They also demonstrated ranging and localization of subjects using an array of PIR sensors. The analog output of the sensor was characterized by varying speed, width, and distance of the subject from the PIR sensor. A model was proposed in order to relate the distance of the subject from the PIR sensor to the peak-to-peak output voltage. It was found that the peak-to-peak output voltage increases as the distance between the subject and the PIR sensor increases, but this increase occurs only up to a certain distance after which the output voltage decreases. The time spent by the subject in the conical FoV increases with distance and should result in a larger peak-to-peak voltage. On the other hand, since the IR rays are absorbed by the environment, the amount of IR received at the PIR sensor decreases as the distance of the subject from the PIR sensor increases. These effects were shown to result in a Gaussian relationship between the peak-to-peak output voltage and distance. Better understanding of this relationship will be key to using PIR sensors for localization.

In [7], a non-injective function is used to express this relationship, i.e. more than one (in this case two) distances map to the same peak-to-peak output voltage value. A bijective function for modeling the output characteristic of the PIR sensor would eliminate any ambiguity in mapping the output voltage to distance. Localization with PIR sensors will then be a range-based technique, without the need for any active transmitter because the human body emits IR, and the PIR sensors act as receivers. This reduces the cost and power consumption of the PIR-based localization system.

Fraden in [11] (Chapter 6) proposed a model for the PIR motion detectors. We describe the working principle of a PIR sensor in Section 2. Fraden's model is based on the following assumptions: the subject has uniform temperature distribution and is a diffuse emitter, image formed on the sensing element is always sharp irrespective of the distance between the subject and the sensor, and the surroundings and the subject are ideal emitters and absorbers. The model is derived by considering the rate of change of temperature of the sensing element (due to the subject), its thermal capacity, and the absorbed thermal power. Fraden's model is given by:

$$i \approx \frac{2Pa\sigma\gamma}{\pi hc} bT_a^3 \frac{(T_b - T_a)}{L^2} \quad (1)$$

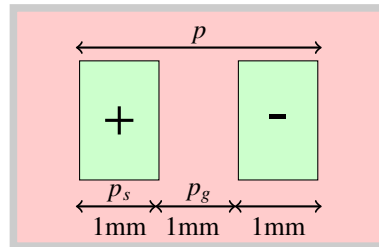


Figure 1: Sensing elements of a PIR sensor.

where i represents the current generated by the sensor, P the sensor's pyroelectric coefficient, a is area of the lens, σ is the Stefan-Boltzmann constant, γ is the lens efficiency, h is thickness and c the specific heat of the sensing material, b is the effective surface area of the subject, T_a is the sensor's temperature, T_b is the surface temperature of the subject, and L is the distance between the subject and the sensor. Theoretical and experimental results for the variation of the output voltage with distance between the sensor and the subject were shown to match reasonably well except at very short distances where the measured voltage was found not to go as high as the calculated curve.

The model proposed in [11] is based on parameters which are difficult to measure experimentally and information regarding these parameters is not available in the datasheet of PIR sensors. This model does not account for the effect of Fresnel lens and the speed of movement of the subject. In addition, it does not address the simulation of analog sensor response (as a function of time) when a subject moves through the FoV of the PIR sensor.

In this paper, we present a model that is based on the overall working principle of the PIR sensor and enables better understanding of the sensor's analog output as different subjects move across its FoV. We will demonstrate that this model is easier to apply and is based on parameters that can be determined via simple experiments. The proposed model considers parameters such as the distance of the subject from the PIR sensor, width and speed of movement of the subject, in order to predict the analog output of the PIR sensor. PIR sensors available in the market come with different types of Fresnel lens depending on the intended application. Fresnel lens is a collection of lenslets capable of regulating the number of zones, range, and angle of coverage of the PIR sensor. The model presented here is able to capture these properties of the Fresnel lens.

The rest of the paper is organized as follows. In Section 2 we discuss the working principle of the PIR sensor. Section 3 and 4 present the formulation and validation of the PIR sensor model, respectively. In Section 5 we discuss some of the potential applications of the proposed model and Section 6 concludes the paper.

2. Working of a PIR sensor

A PIR sensor consists of two sensing elements as shown in Fig. 1. The sensing elements are of width p_s and are separated by a gap of width p_g . The sensor's Fresnel lens focuses a thermal image on the sensing elements which absorb the thermal energy from the image and convert it into heat. Further, this heat is converted into a minute electric current by the pyroelectric crystalline material.

Fig. 2 shows the PIR sensor (model RE200B [12]) along with the Fresnel lens used for the experiments in this work. For this PIR sensor $p_s = p_g = 1$ mm. The sensing elements are

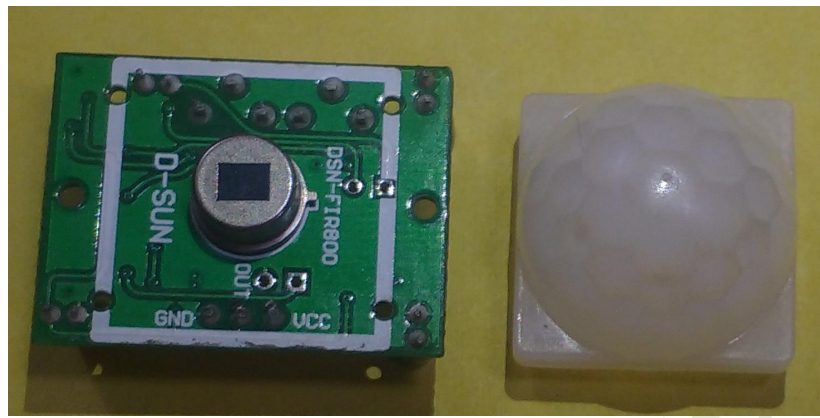


Figure 2: PIR sensor and the Fresnel lens used in this work.

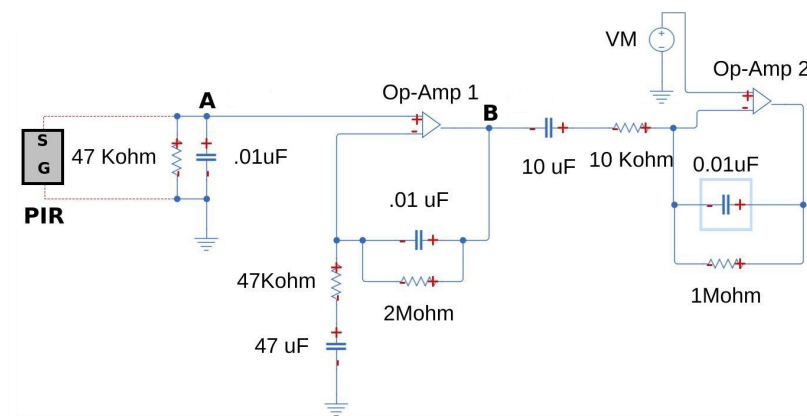


Figure 3: Typical amplifier circuit used with a PIR sensor [13].

sensitive to IR radiation and are placed beneath a rectangular window or slot on its enclosure. The whole sensor is housed in an air tight metal capsule to protect it from noise, and temperature and humidity fluctuations. An IR emitting subject entering the sensor's FoV will activate the first sensing element and then the other element. Other IR sources such as ambient IR will affect both the elements simultaneously and thus cancel out. The subject creates a temperature difference between the sensing elements which is converted to an electrical signal by the sensor. As the subject moves away from the PIR sensor, the intensity of the IR radiation incident on the sensing elements decreases which in turn reduces the temperature difference resulting in an electrical signal of lower amplitude. The electrical signals are in microvolts and have to be amplified before they can be used for triggering any device. For this purpose, the PIR sensor board includes an amplifier (such as the integrated circuit amplifier BIS001 [13]) as shown in Fig. 3. The amplified signal (output of Op-Amp 2) is quantized with the help of two comparators and is converted to digital form (the comparator circuit is not shown).

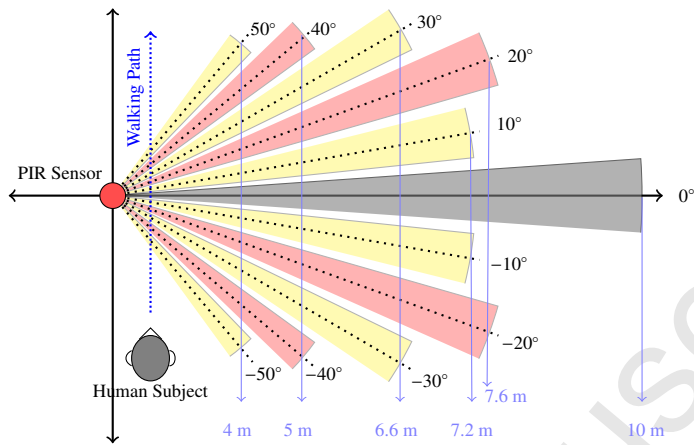


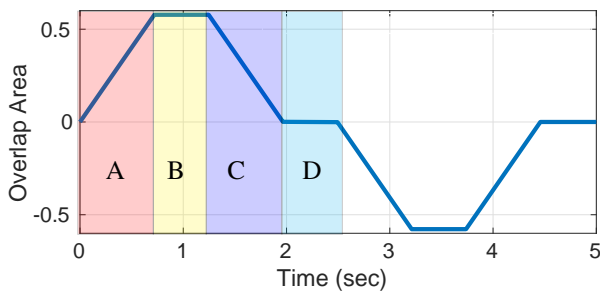
Figure 4: Field of view of the PIR sensor with the Fresnel lens.

PIR sensors are fitted with a Fresnel lens in order to extend its FoV. Fresnel lens, rather than a simple lens, is used as it can provide a large aperture and short focal length without a significant change in the size and mass of the material. The sensing elements are placed exactly at the focus of the lens. The conical FoV can be made longer and narrower or shorter and broader by using different kinds of lens. FoV of the Fresnel lens used in this work is shown in Fig. 4. The sensor's FoV has eleven sectors spanning from -50° to $+50^\circ$ with the detection range varying from 4 m to 10 m. Each sector has a viewing angle (ψ) of 8° and the image formed by the sectors fall on the two sensing elements.

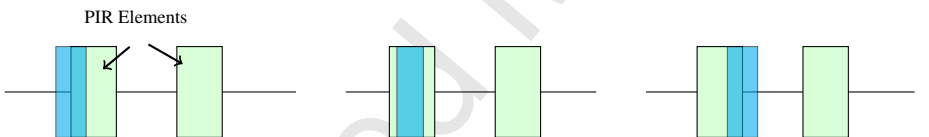
The sensor produces a positive output when image of the subject falls mainly on the positive sensing element ("+") and produces a negative output when the image falls mainly on the negative sensing element ("−") (refer Fig. 1). Therefore when a subject crosses a sector from one end to the other the sensor produces a full output swing as depicted in Fig. 5(a). Without loss of generality, we consider the subject's image to be rectangular in shape. The shape of the image does not change with distance or angle so the nature of the output is unaffected when a particular class of subjects (such as humans) are considered. The sensor output will be zero when the image occupies the same area on the two sensing elements or falls entirely in the region between the two elements.

The height of the image or of the sensing elements does not affect the shape of the output and only results in scaling. Fig. 5 shows the overlapping area of the subject's image with the sensing elements (which is proportional to the sensor output) when a subject moves from one end to the other of the FoV, as shown in Fig. 4. Fig. 5(b)-5(e) show the position of the subject's image over the sensing elements corresponding to parts A-D of the waveform in Fig. 5(a). For the output shown in Fig. 5(a), the subject crosses the FoV at a distance of 7.61 m with only one sector, corresponding to $\theta = 0^\circ$, being active. Similar outputs are obtained for cases where the PIR sensor is without a lens or only a single sector is active. The rate of increase or decrease of the output, and the time duration of the positive and negative cycles depends on the width and speed of movement of the subject.

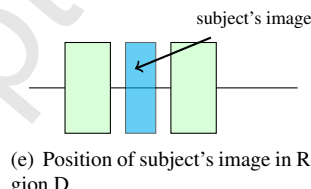
When a subject crosses the sensor's FoV, its image falls on the sensing elements. The rela-



(a) Variation of the output as the subject's images passes over the PIR elements.



(b) Position of subject's image in Region A. (c) Position of subject's image in Region B. (d) Position of subject's image in Region C.



(e) Position of subject's image in Region D.

Figure 5: Working of a PIR sensor when a subject passes through its FoV.

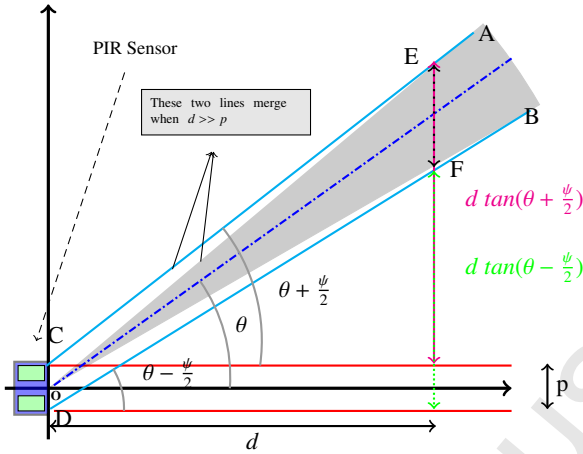


Figure 6: Relation between the actual width of the subject and the width of the image on the PIR elements.

tionship between the width of the subject (w_s) and its image (w_i) is given by:

$$w_i = w_s \times \frac{p}{[d \tan(\theta + \frac{\psi}{2}) + p - d \tan(\theta - \frac{\psi}{2})]} \quad (2)$$

where d is the distance of the subject from the PIR sensor, θ the central angle of the sector, ψ is the viewing angle, and $p = 2p_s + p_g$ (refer Fig. 6). If \overline{EF} is the width of the subject then \overline{CD} is the width of its image. Therefore the actual width of a subject inside the sector will be scaled by the factor $\frac{p}{\overline{EF}}$. To calculate the value of \overline{EF} , point O is replaced by a line segment CD of length spanning the two sensing elements together with the gap between them. Instead of considering the conical FoV ($\angle AOB$) we assume it to be a trapezoid $CDBA$. It can also be assumed that $OA \equiv CA$ and $OB \equiv DB$ as $d \gg p$. From (2), it is clear that as the subject moves away from the PIR sensor, the width of its image decreases. When the image width becomes less than $\frac{p}{3}$ (assuming $p_s = p_g$), the maximum sensor output voltage will be proportional to w_i . This is because the maximum output voltage corresponds to the case when the difference between the area of the sensing elements overlapping with the image is maximum. Beyond a certain distance, the width of the image becomes so small that the response of the sensing elements is insignificant and the output is almost zero. The width of the image also determines the shape of the output curve as explained below and illustrated in Fig. 7:

- $w_i \geq p$: Each half (positive and negative) of the output waveform is trapezoidal in nature (refer Fig. 7(a)) with the maximum value being attained when the image completely covers only one of the sensing elements. The output goes to zero when the image simultaneously covers both the sensing elements completely. The wider the image, longer is the duration between the positive and negative halves.
- $p_s \leq w_i \leq p$: Each half of the output is a distorted trapezoid as shown in Fig. 7(b) (except when $w_i = p_s + p_g$). The distortion is on the falling edge of the positive and negative cycles due to the fact that parts of the image overlap with the positive and negative sensing elements, and these parts do not have the same overlapping area. When $w_i = p_s + p_g$,

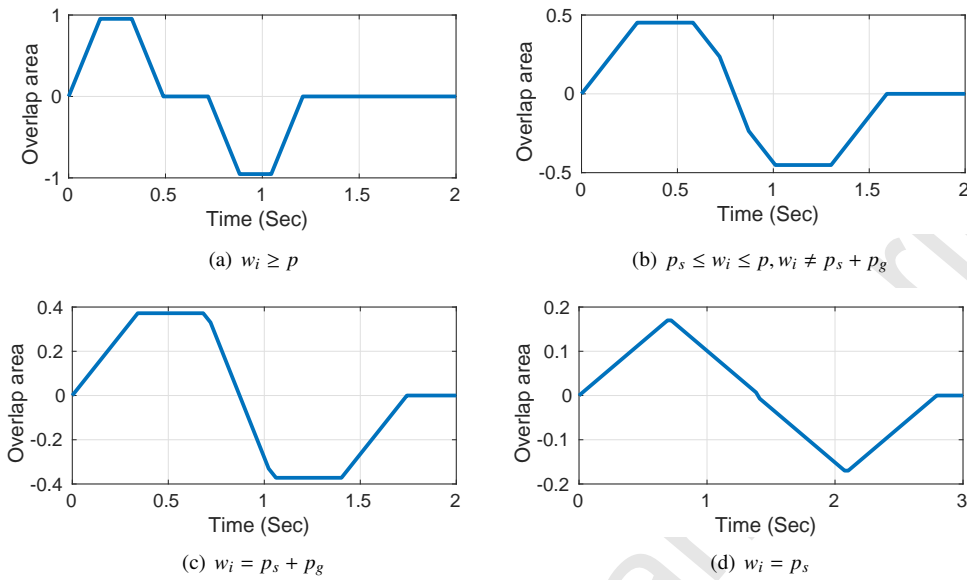


Figure 7: Output of the PIR sensor corresponding to different w_i when only the central sector of the FoV is active.

each half of the output becomes trapezoidal without any distortion (refer Fig. 7(c)). This is because the rate of increase and decrease of the image overlapping areas with the two sensing elements are the same.

- $w_i = p_s$: Each half of the output is a triangular waveform assuming $p_s = p_g$ (refer Fig. 7(d)).
- $w_i \leq p_s$: Each half of the output waveform is trapezoidal and has a maximum value that is proportional to w_i (refer Fig. 5).

3. Mathematical Model for the PIR sensor

Based on the working principle of the PIR sensor presented in the previous section, the analog sensor output depends on the following parameters:

- difference in the overlapping area (a) of the subject's image with the two sensing elements,
- distance of the subject from the PIR sensor (d),
- time spent by the subject in the FoV of the PIR sensor (t), and
- central angle of the sector the subject is traversing (θ).

The PIR sensor output voltage V_{out} can be expressed mathematically as:

$$V_{\text{out}}^i = \beta a t d^{-\alpha} \left(1 + \frac{|\theta_i|}{10}\right)^{-\gamma} \quad (3)$$

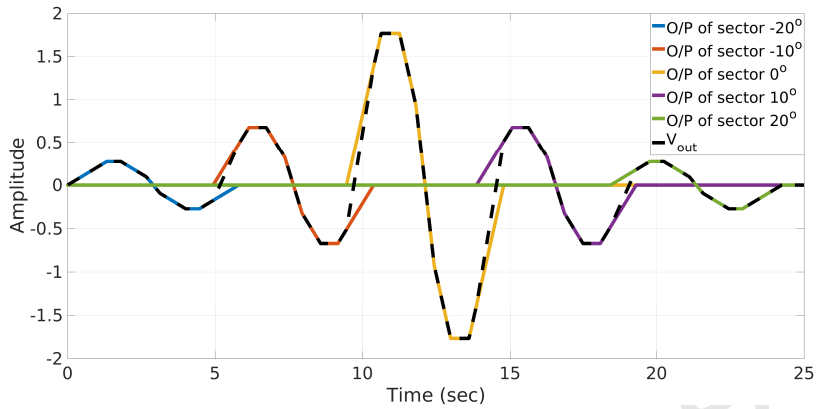


Figure 8: PIR model output when a subject of width 0.5 m, at a distance of 7 m from the PIR sensor, moves at 0.277 m/s.

where V_{out}^i is the sensor output as the subject traverses the i^{th} sector with central angle θ_i , β is a scale factor, and α and γ are tuning parameters of the model ($\alpha \geq 0, \gamma \geq 0$). i represents the sector of the sensor's FoV that is currently active or being traversed. The parameter t is inversely proportional to the speed of movement of the subject. A slow moving subject will spend more time in the FoV than a fast moving subject with the sensing elements being exposed to IR radiation for a longer duration in the former case. Thus V_{out} is inversely proportional to the speed of movement of the subject.

IR emitted by the subject gets absorbed by the surrounding air, so as d increases the intensity of the IR radiation falling on the sensing elements decreases, reducing the output voltage. This variation with distance is modelled by the factor $d^{-\alpha}$ where $\alpha \geq 0$. The subject is analogous to a light source with luminosity L and the flux density is given by $F = \frac{L}{A}$ where A is the surface area of the illuminated surface. In this case, the surface is a sphere with the light source at the center. If we assume an omnidirectional point source then $A = 4\pi r^2$ where r is the distance of the light source from the surface. Thus, $F \propto r^{-2}$. This suggests that the parameter α in (3) will be close to 2. A similar relationship is observed in the temperature on the Earth's surface as its distance from the sun varies [14].

The amplitude of the sensor output also depends on the sector currently being traversed by the subject. The Fresnel lens is spherical in nature and its focal length is of the order of a few millimeters, thus all the rays from the subject incident on the lens are almost parallel to each other. The rays that pass through the central part of the Fresnel lens and fall on the sensing elements do not undergo any bending. However, the off-center rays undergo refraction and additional power loss due to refraction. These rays, compared to the central rays, contribute less in illuminating the sensing elements. This effect is captured by the hyperbolic relationship between V_{out} and θ in (3). As the sector angle increases the sensor's response decreases. By using the term $(1 + \frac{|\theta|}{10})^{-\gamma}$, we shift the hyperbolic function $(\frac{|\theta|}{10})^\gamma$ in order to avoid the problem of $V_{\text{out}} \rightarrow \infty$ as $\theta \rightarrow 0$. Note that $(\frac{|\theta|}{10})$ can be replaced by $|\theta|$ while affecting only the value of γ .

The authors in [15] discuss the relationship between the lens efficiency and the angle of incidence of the rays. This relationship can be approximated by a Gaussian curve with mean at $\theta = 0^{\circ}$. Thus the term $(1 + \frac{|\theta|}{10})^{-\gamma}$ can be replaced by a term of the form $e^{-\gamma\theta^2}$ without a significant

change in the model (3) behavior. For low values of the variance ($\frac{1}{\gamma}$) these terms are very similar. Importance of the parameter θ can also be inferred from the variation of the Earth's surface temperature with the latitude [16, 17]. Finally, β is a scale factor that is determined empirically.

Objects moving through the entire FoV of the PIR sensor, as shown in Fig. 4, will traverse across each of the sectors, with each sector resulting in a sensor response given by (3). The overall sensor output is considered to be the superposition of the output signal due to each sector, i.e. $V_{\text{out}} = \sum_i V_{\text{out}}^i$. Fig. 8 illustrates this for a subject of width 0.5 m at a distance of 7 m from the PIR sensor and moving at a speed of 0.277 m/s. The height of the individual peaks in V_{out} depends on the w_s and d . Destructive interference may occur between the different V_{out}^i due to which some of the peaks may be attenuated. Since the overall FoV of the PIR sensor is symmetric and the subject is travelling parallel to the sensor's axis, V_{out} will also be symmetric.

Let V_{out} and $V_{\text{out}}^{\text{amp}}$ represent the signal at points A and B in Fig. 3. The output of the second amplifier can also be used, however in some cases this output gets clipped or saturates due to over amplification. Thus in the rest of this paper we consider the output at point B as the sensor's analog output.

The tuning parameters α , β , and γ are determined empirically by matching the simulated model output with the sensor output obtained from the experiments. The resultant model is:

$$V_{\text{out}}^i = 11atd^{-1.5} \left(1 + \frac{|\theta_i|}{10}\right)^{-10} \quad (4)$$

where α accounts for the rate of decrease of the output voltage with distance, β is a scale factor, and γ affects the amplitude of the peaks of V_{out} .

4. Performance Evaluation of the Mathematical Model

Experiments were carried out for evaluating the performance of the mathematical model and comparing the model output with the experimental results. During these experiments, a human subject of height 1.72 m was made to walk at different distances from a PIR sensor across its FoV. Fig. 9 shows the experimental setup used for recording data from the PIR sensor. The sensor was placed on a tripod at a height of 1.40 m and powered by a 5 V lithium polymer battery. The output of the PIR amplifier circuit was connected to Channel 1 of the mixed signal oscilloscope (MSO). The subject moved transverse to the PIR sensor and along a straight line path as shown in Fig. 4. Since the subject was wearing a full sleeve shirt and trouser the only source of IR radiation was the face, therefore the width of the subject is considered to be 0.2 m. It can be seen from Fig. 10 that the main source of IR radiation from a clothed human body is the face. The walking speed of the subject was measured using a stop watch.

Fig. 11 shows a comparison of the sensor output from experiments and the simulated model output for a subject walking at different distances from the PIR sensor. The simulated output is obtained by superimposing the outputs for each of the active sectors using (4) and passing it through the amplifier circuit (Fig. 3) simulated in Simulink. The experimental output waveform is recorded at point B on the PIR sensor circuit using a mixed signal oscilloscope. Most of the commercially available PIR sensors have similar signal conditioning circuits with minor changes in the values of resistors and capacitors.

Fig. 11(a) shows the output waveform corresponding to the subject at a distance of 1 m from the PIR sensor and moving at a speed of 0.361 m/s. In this case, the model output and the experimental result do not exhibit a good match. However, time duration of the event (subject passing

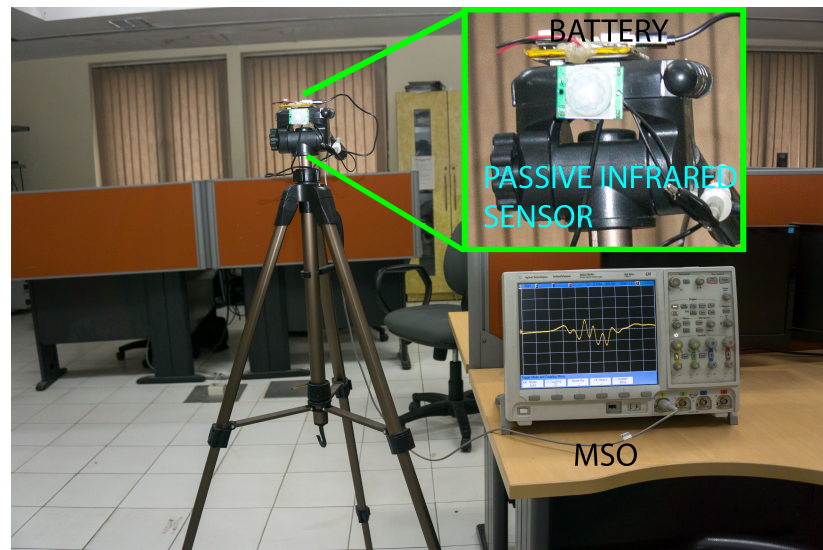


Figure 9: Experimental setup for recording the analog output of the PIR sensor.



Figure 10: Thermal image of a subject walking transverse to the camera [18].

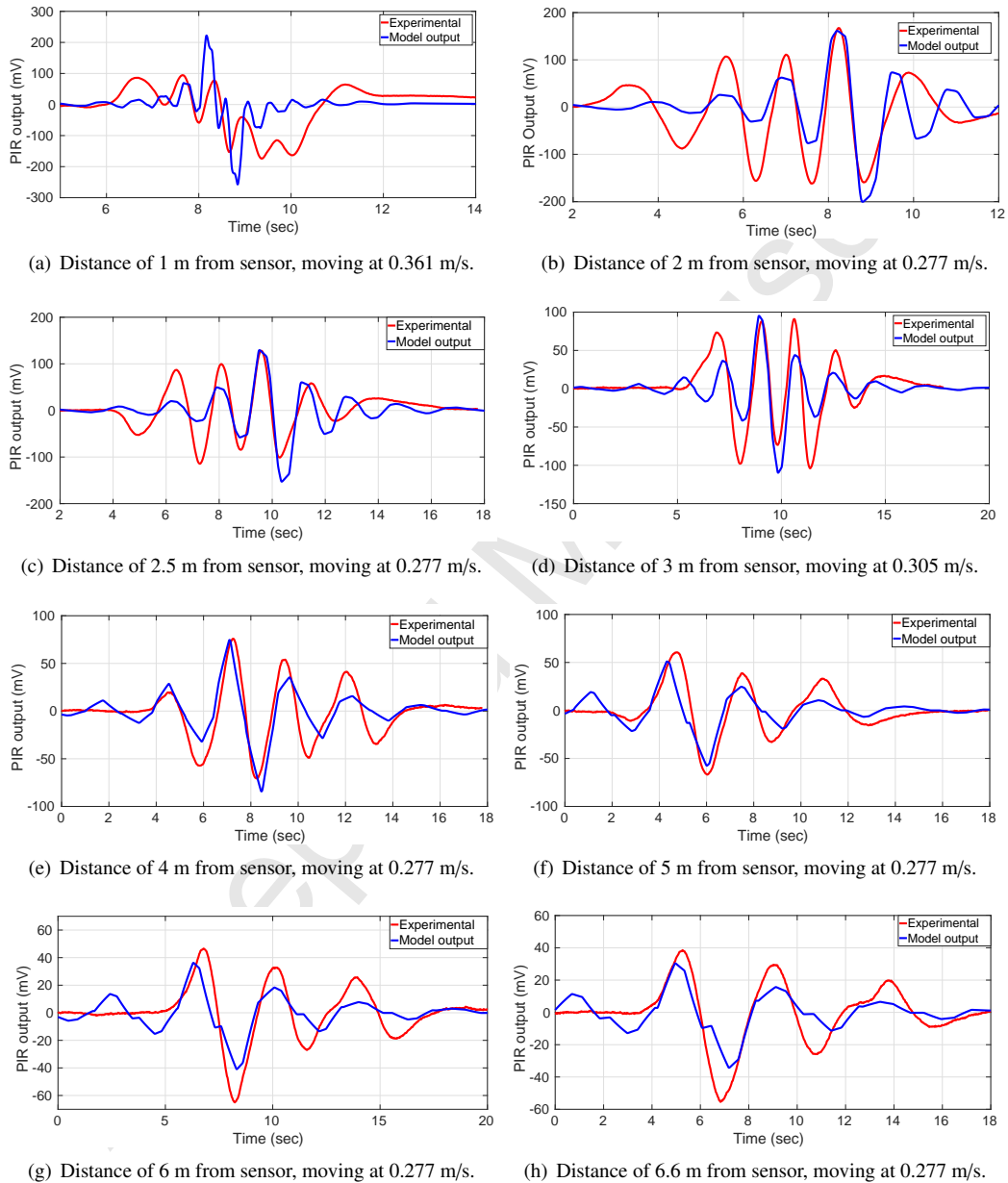


Figure 11: Experimental and simulated PIR sensor outputs with the subject moving at different distances from the sensor.

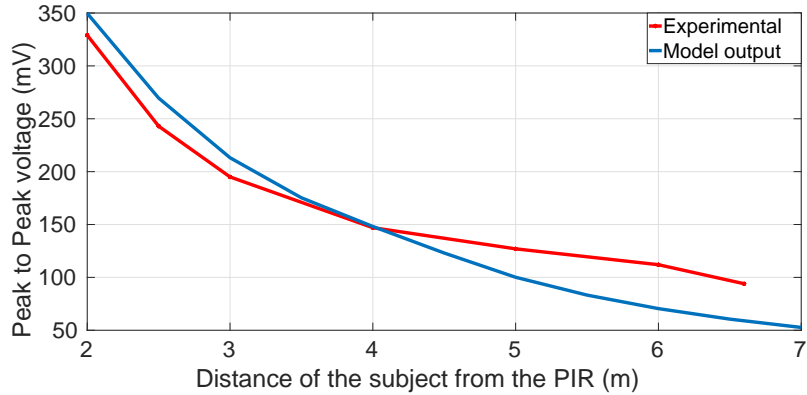


Figure 12: Peak-to-peak sensor output voltage as a function of the distance d with the subject moving transversely to the sensor at a speed of 0.277 m/s.

through the FoV) is almost the same in both results with the main lobe showing a reasonable match though it is attenuated in the experimental output. The mismatch may be due to fact that the subject is moving very close to the sensor resulting in destructive interference among the sectoral outputs. As the event duration is relatively short, the sensor response time could also have an impact on the output waveform. At distances of 2 m and above, the model output shows a good match with the experimental waveform. In Fig. 11(b)-11(h), the main lobe of the waveforms show a good match in terms of the shape and amplitude with only small mismatches in the side lobes. As we increase the distance between the subject and the PIR sensor, the FoV span from one side to the other also increases (e.g. at 6.6 m distance the FoV span is 9.2 m). Due to space constraints inside the laboratory, for distances of 5 m and above, the experimental output could only be recorded up to the secondary and tertiary peaks to the right of the main lobe. The sensor output is symmetric on either side of the main lobe which is observed in the model outputs. In some cases the symmetry may not be apparent due to the time axis having been clipped. The experiment could not be performed at distances larger than 6.6 m due to the space constraints in the laboratory.

Fig. 12 shows the variation of the peak-to-peak sensor output voltage (V_{pp}) as a function of the distance of the subject from the PIR sensor (d). Results from the experiments and the model show a reasonable match. Results at $d = 1$ m have not been included in Fig. 12 due to the discrepancy observed in Fig. 11(a). Such a behavior of the output voltage when the subject is very close to the sensor was indicated in [11] as well.

4.1. Sensor Detection Range and Ambient Temperature

Generally the detection range of a PIR sensor depends on the size and thermal properties of the subject, ambient temperature, and the amplifier circuitry. Table 1 lists the detection range of different PIR sensors available in the market. The PIR sensors generate a trigger only when the sensor output voltage exceeds a threshold. If the width of the subject's image is too thin, it will not generate a significant temperature difference between the sensing elements, resulting in a low output voltage. This low output may not trigger the sensor limiting the detection range.

Table 1: Detection range of the PIR sensors available in the market.

Model name	Range (m)
PIR Mini Sensor (Parallax) [19]	3.65
PIR Sensor (RE 200B) (Adafruit) [12]	7.00
PIR Sensor (Rev B) (Parallax) [20]	9.14
Wide Angle PIR Sensor (Parallax) [21]	9.14

The detection range also depends on the ambient temperature. The sensor output is determined by the temperature difference between the sensing elements. As the ambient temperature increases, temperatures of the sensing elements also increase, and the temperature difference between the elements (when an image is incident on them) decreases. This results in a lower sensor output voltage and reduced range with increase in the ambient temperature. Datasheet of PIR sensors (e.g. [22]) typically include details on the effect of ambient temperature on the sensor's detection range. The model proposed in this paper can be modified to include the effect of ambient temperature as shown below:

$$V_{out} = \beta atd^{-\alpha} \left(1 + \frac{|\theta|}{10}\right)^{-\gamma} T^\kappa \quad (5)$$

where T is the ambient temperature in Kelvin and κ is a tuning parameter. In order to estimate the value of κ , one would have to perform the experiment by varying the ambient temperature, which would be challenging.

4.2. Speed of Movement of the Subject

Fig. 13 shows the effect of the speed of movement of the subject on the peak-to-peak sensor output voltage. The speed of the subject was measured using a stop watch. The human subject traversed the FoV at distances ranging from 2 m to 7 m from the sensor at three different speeds, with each experiment being repeated three times. The subject walked/ran in front of the PIR along the path shown in Fig. 4. The speed was calculated by measuring the distance between the start and end points, and the time taken to traverse it. An increase in the speed of the subject implies less time being spent by the subject in the sensor's FoV, captured by the parameter t in (3), resulting in a decrease in the sensor output voltage. From (3), it can be shown that $V_{pp}^i \propto \frac{d^{-\alpha}}{s}$ as $s \propto \frac{1}{t}$, where s is the speed of movement of the subject. Other terms such θ and a can be ignored as θ affects only the amplitude of the output and a affects the shape of the output waveform. The peak-to-peak output voltage is given by $V_{pp} = \max(V_{out}) - \min(V_{out})$ where $V_{out} = \sum_i V_{out}^i$, and unless the superposition of the individual sector outputs results in destructive interference, V_{pp} will equal the difference between the maximum and minimum values of V_{out}^i corresponding to $\theta_i = 0$. Thus, $\frac{dV_{pp}}{ds} \Big|_d \propto -\frac{d^{-\alpha}}{s^2}$ and as the distance d increases, we have:

$$\frac{dV_{pp}}{ds} \Big|_{d=d_1} > \frac{dV_{pp}}{ds} \Big|_{d=d_2} \text{ for } d_2 > d_1. \quad (6)$$

In Fig. 13, it is observed that the rate of change of the peak-to-peak output voltage with speed decreases as the distance of the subject from the PIR sensor increases, which is in agreement with (6). Note that the peak-to-peak voltage in Fig. 13 and Fig. 12, corresponding to a speed of

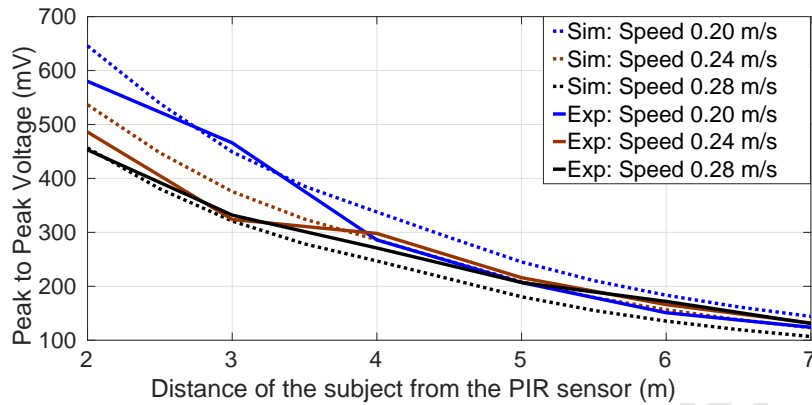


Figure 13: Peak-to-peak sensor output voltage with the subject moving through the FoV at different speeds.

0.277 m/s, do not match as these experiments were conducted in different environments. The PIR sensor model parameters change with the change in environment. It is also noted from Fig. 13 that as the speed of the subject increases, the peak-to-peak output voltage decreases.

4.3. Sensor Response Time

The proposed model does not account for the response time of the sensor explicitly as there is no obvious way to estimate this parameter. To understand the effect of sensor response time, we record the sensor output as subject moves through the FoV at a distance of 3 m from the sensor at different speeds. Fig. 14 shows the simulated and experimental output waveforms as the subject moves at three different speeds ranging from 0.277 m/s to 1.388 m/s. In Fig. 8 and Fig. 11 the absolute voltage at the (positive and negative) peaks of the output waveform increases as the subject moves towards the center of the FoV. However, in Fig. 14, the experimental waveforms have a first negative peak (from left) that is larger than the second negative peak. In addition Fig. 14(b) and Fig. 14(c), we observe that the experimental waveforms do not show a good match with the model output. The sensor does not seem to have sufficient time to complete the first output voltage swing following the initial negative slope. The voltage swing due to the second sector starts before completion of the first swing and thus the overall output oscillates with a negative bias. Another reason for the mismatch could be the subject's speed being non-uniform and the speed indicated (and used in the model) is the average speed. The waveforms in Fig. 14(a) show a good match as the subject in this case is moving at a lower speed allowing sufficient time for the individual sector responses.

Even though the model does not explicitly capture the sensor's response time, the model includes the following which form a part of the response time: (i) start and end times (or duration) of an event, (ii) relation between the peak-to-peak voltage and speed of the subject, (iii) number of positive and negative peaks, and (iv) duration of the peaks.

5. Application of the Proposed Mathematical Model

We have applied the proposed model for PIR-based indoor localization [23]. Indoor localization has been an active area of research for many years, but a solution seems elusive that can

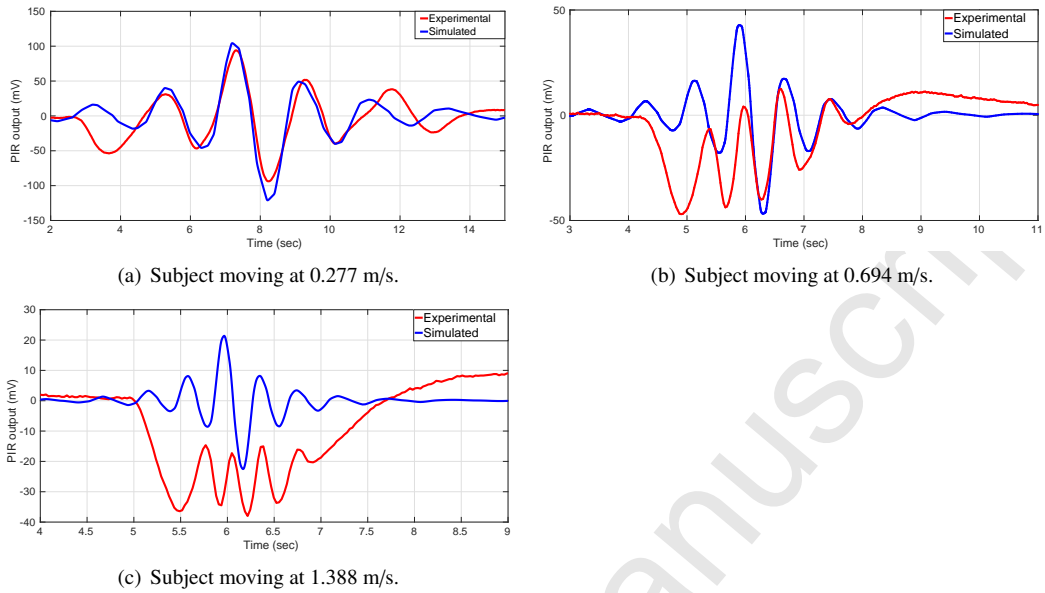


Figure 14: Experimental and simulated sensor outputs with the subject moving through the FoV at different speeds.

recreate the experience Global Positioning System (GPS) provides in outdoor environments [24]. GPS-based systems do not work indoors and consume large amounts of power. Various technologies have been used for human localization in indoor environments such as camera, radio frequency (RF) including ultra-wideband (UWB), ultrasonic, and seismic. Most of these sensors or transceivers are expensive and require high computational power for processing the raw signals. On the other hand, PIR sensors are economical, low power, and tend to require low computational power. In [23], we presented a localization technique based on the proposed model and support vector regression. Using four PIR sensors, we demonstrated the ability to localize a human subject in a $7 \text{ m} \times 7 \text{ m}$ area with a root mean square error of 0.65 m.

We have also developed a simulator in Matlab together with a graphical user interface (GUI), which can be used to simulate the analog response of a PIR sensor with different properties and Fresnel lens. This software tool will be an aid to the PIR sensor and Fresnel lens designers for simulating the sensor and lens response before building them for specific applications [25].

6. Conclusion

In this paper, we have presented the working principle of a PIR sensor and based on this proposed a mathematical model for simulating the sensor's analog output or response under different scenarios. The sensor output waveform generated by the model shows a good match with the experimentally observed waveforms. A typical PIR sensor has two IR sensitive elements that are triggered when an IR emitting object moves through its FoV. The Fresnel lens divides the FoV of the sensor into several sectors. We observed that the output of the PIR sensor depends on four parameters namely, the overlapping area of the subject's image on the sensing elements, time spent by the subject in the sensor's FoV, distance of the subject from the sensor, and the angle of the sector which the subject is currently traversing. We performed experiments where a human

subject moves through the FoV at different distances from the sensor. The model generated results have been validated against the experimental results and display a good match. The proposed sensor model and the simulator software would be useful for sensor and lens designer as well as application developers working with PIR sensors.

7. Acknowledgement

B. Mukhopadhyay is supported through the Visvesvaraya PhD Scheme fellowship from the Ministry of Electronics and Information Technology (MEITY), Govt. of India.

Reference

- [1] A.-J. Garcia-Sanchez, F. Garcia-Sanchez, F. Losilla, P. Kulakowski, J. Garcia-Haro, A. Rodriguez, J.-V. Lopez-Bao, F. Palomares, Wireless sensor network deployment for monitoring wildlife passages, *Sensors* 10 (8) (2010) 7236–7262.
- [2] J.-S. Fang, Q. Hao, D. J. Brady, M. Shankar, B. D. Guenther, N. P. Pitsianis, K. Y. Hsu, Path-dependent human identification using a pyroelectric infrared sensor and Fresnel lens arrays, *Opt. Exp.* 14 (2) (2006) 609–624.
- [3] P. Zappi, E. Farella, L. Benini, Enhancing the spatial resolution of presence detection in a PIR based wireless surveillance network, in: *IEEE Conf. Advanced Video and Signal Based Surveillance*, 2007, pp. 295–300.
- [4] R. Rana, D. Austin, P. G. Jacobs, M. Karunanithi, J. Kaye, Gait velocity estimation using time-interleaved between consecutive passive IR sensor activations, *IEEE Sensors J.* 16 (16) (2016) 6351–6358.
- [5] X. Jin, S. Sarkar, A. Ray, S. Gupta, T. Damarla, Target detection and classification using seismic and PIR sensors, *IEEE Sensors J.* 12 (6) (2012) 1709–1718.
- [6] N. Li, Q. Hao, Multiple human tracking with wireless distributed pyro-electric sensors, in: *Proc. SPIE*, Vol. 6940, 2008, pp. 694033–694033–12.
- [7] S. Narayana, R. V. Prasad, V. S. Rao, T. V. Prabhakar, S. S. Kowshik, M. S. Iyer, PIR sensors: Characterization and novel localization technique, in: *Int. Conf. Information Processing in Sensor Networks (IPSN)*, 2015, pp. 142–153.
- [8] P. Zappi, E. Farella, L. Benini, Tracking Motion Direction and Distance With Pyroelectric IR Sensors, *IEEE Sensors J.* 10 (9) (2010) 1486–1494. doi:10.1109/JSEN.2009.2039792.
- [9] G. Mokhtari, Q. Zhang, G. Nourbakhsh, S. Ball, M. Karunanithi, BLUESOUND: A New Resident Identification Sensor – Using Ultrasound Array and BLE Technology for Smart Home Platform, *IEEE Sensors J.* 17 (5) (2017) 1503–1512.
- [10] Q. Hao, F. Hu, Y. Xiao, Multiple human tracking and identification with wireless distributed pyroelectric sensor systems, *IEEE Systems J.* 3 (4) (2009) 428–439.
- [11] J. Fraden, *Handbook of Modern Sensors: Physics, Designs, and Applications*, 4th Edition, Springer, 2010.
- [12] PIR Motion Sensor – Adafruit, <https://www.adafruit.com/product/189>, accessed: 2018-02-28.
- [13] Micro Power PIR Motion Detector IC BISS0001, <https://cdn-learn.adafruit.com/assets/assets/000/010/133/original/BISS0001.pdf>, accessed: 2017-04-04.
- [14] M. Donabedian, D. G. Gilmore, Spacecraft thermal control handbook, *Cryogenics* 2 (2003) 603.
- [15] L. Jing, H. Liu, H. Zhao, Z. Lu, H. Wu, H. Wang, J. Xu, Design of novel compound Fresnel lens for high-performance photovoltaic concentrator, *Int. J. of Photoenergy* 2012.
- [16] J. Hansen, S. Lebedeff, Global trends of measured surface air temperature, *J. of Geophysical Research* 92 (13) (1987) 345–13.
- [17] Global Surface Temperature Distribution, <http://www.physicalgeography.net/fundamentals/7m.html>, accessed: 2017-04-04.
- [18] Thermal images of our everyday life, <http://vuving.com/thermal-images-of-our-everyday-life/>, accessed: 2017-04-04.
- [19] Wide Angle PIR Sensor – Parallax, <https://www.parallax.com/product/28032>, accessed: 2018-02-28.
- [20] PIR Sensor (Rev B) – Parallax, <https://www.parallax.com/product/555-28027>, accessed: 2018-02-28.
- [21] PIR Mini Sensor – Parallax, <https://www.parallax.com/product/28033>, accessed: 2018-02-28.
- [22] PIR Sensor Product Guide v2.3 – Parallax, <https://www.parallax.com/sites/default/files/downloads/555-28027-PIR-Sensor-Product-Guide-v2.3.pdf>, accessed: 2018-02-28.
- [23] B. Mukhopadhyay, S. Sarangi, S. Srirangarajan, S. Kar, Indoor localization using analog output of pyroelectric infrared sensors, in: *2018 IEEE Wireless Commun. and Netw. Conf. (WCNC)*, Barcelona, Spain, 2018, pp. 1617–1622.

- [24] D. Lymeropoulos, J. Liu, The microsoft indoor localization competition: Experiences and lessons learned, *IEEE Signal Processing Magazine* 34 (5) (2017) 125–140.
- [25] B. Mukhopadhyay, S. Sriranganjan, S. Kar, Software tool for modeling the analog response of passive infrared sensor, Available online: <https://in.mathworks.com/matlabcentral/fileexchange/67325-software-tool-for-modeling-the-analog-response-of-passive-infrared-sensor>.

Author Biographies

Bodhibrata Mukhopadhyay received his Master of Science (Research) in Telecommunication from Indian Institute of Technology Delhi (IITD) in 2015. He is now a PhD student in the department of electrical engineering in IITD. The topic he is working on is localization in ad hoc wireless sensor network. He is one of the co-founders of a startup named "Suxma Systems". It researches and develops IOT based dairy equipments and bio-medical equipments. His research interests include embedded system, signal processing, machine learning and bio-medical electronics.

Seshan Srirangarajan received the B.E. degree from the University of Mumbai, India in 2001, and the M.S. and Ph.D. degrees from the University of Minnesota in 2005 and 2008, respectively, all in Electrical Engineering. He is currently an Assistant Professor in the Department of Electrical Engineering at the Indian Institute of Technology Delhi. Prior to this he was an IRCSET/Intel Postdoctoral Fellow with the Nimbus Centre for Embedded Systems Research at the Cork Institute of Technology, Ireland. From 2008 to 2011, he was a Research Fellow with the Intelligent Systems Center at the Nanyang Technological University, Singapore. In 2005-06, he was with the Wireless Technologies Group at Honeywell Technology Center, Minneapolis, Minnesota, as an intern. His research interests span the broad areas of signal processing and wireless communications with current focus being on positioning in wireless networks, sensor networks, and array signal processing.

Subrat Kar graduated with Honours in Electrical & Electronics Engineering from the Birla Institute of Technology & Science, Pilani in 1987. He holds a Doctoral Degree in Electrical Communication Engineering from the Indian Institute of Science, Bangalore (1991). He has been with the International Center for Theoretical Physics, Trieste as a Post-Doctoral Fellow (1991-1994). Presently he is a Professor at the Department of Electrical Engineering, Indian Institute of Technology Delhi where he is also the Ram and Sita Sabnani Chair Professor. He is one of the co-founders of a startup named "Suxma Systems". It researches and develops IOT based dairy equipments and bio-medical equipments. His research areas are in optical communication, switching, access technologies, telecom protocols, embedded systems and high speed networks. As a member of the Optoelectronics and Optical Communication research group, he works in the area of non-linear optical CDMA networks, free-space optical communication (ground-satellite and inter-satellite) and in ultra-fast optical LSI and fault-tolerant integrated optical switching architectures. His interests also involve formalisms in embedded system design, hardware-software co-design, telecom protocol design and verification tools for telecommunication protocols. He has designed and holds patents in the field of large-scale sensor networks, routing algorithms, macro languages, large scale repository design for sensor data and localization issues in sensor networks.

Highlights

- Mathematical model based on the working principle of the PIR sensor is proposed.
- Better understanding of the sensor output as subject's traverse its field of view.
- Model predicts sensor's analog response matching reasonably well with experiments.
- Parameters include subject's width, distance and speed, sensor and lens properties.
- Simulator for generating PIR sensor output with tunable properties and Fresnel lens.